Journal of Nanostructure in Chemistry
https://doi.org/10.1007/s40097-020-00348-8

ORIGINAL RESEARCH

Optical and electrochemical properties of iron oxide and hydroxide nanofibers synthesized using new template-free hydrothermal method

M. Boufas[1] · O. Guellati[1,2] · A. Harat[1] · D. Momodu[3] · J. Dangbegnon[3] · N. Manyala[3] · M. Guerioune[1]

Received: 30 June 2020 / Accepted: 3 September 2020

Abstract

We report the effect of hydrothermal synthesis conditions on the morphological, optical and electrochemical properties of as-prepared iron oxide (γ-Fe_2O_3) and hydroxide (α-FeOOH) nanostructures. The physico-chemical identification of these Fe-based nanostructures using X-ray diffraction, scanning/transmission electron microscopy, porosity and Raman spectroscopy analyses revealed a temperature-depended phase transformation. A maghemite and goethite iron-based nanostructured formation was observed in nanorod and trigonal nanofiber shape-like morphology with mean diameters ranging from 32 to 50 nm. The textural analysis of the nanofibers confirmed mesoporosity with a specific surface area of ~ 129 $m^2\ g^{-1}$ (in γ-Fe_2O_3) and 23 $m^2\ g^{-1}$ (in α-FeOOH). The electrochemical performance of the iron oxide and hydroxide nanofiber electrodes with and without the addition of activated carbon (AC) was also investigated. The sample electrodes composed of γ-Fe_2O_3, γ-Fe_2O_3/AC, α-FeOOH and α-FeOOH/AC showed remarkable specific capacities of 164 mAh g^{-1}, 330 mAh g^{-1}, 51 mAh g^{-1} and 69 mAh g^{-1} at 1 A g^{-1} gravimetric current. The influence of the phase transformation linked to the synthesis temperature, and the inclusion of an electric double-layer AC material into the nanofibers clearly demonstrates an enhancement in their energy-storage capability. Furthermore, the Fe-based nanofibers exhibited excellent cycling stability with good capacity retention of 73% and 99.8%, respectively, after 2000 cycles at a high 30 A g^{-1} gravimetric current as well as low resistance obtained by impedance spectroscopy analysis. The implication of the results depicts the potential of adopting these γ-Fe_2O_3 nanorods as suitable material electrodes in electrochemical energy-storage devices.

Electronic supplementary material The online version of this article (https://doi.org/10.1007/s40097-020-00348-8) contains supplementary material, which is available to authorized users.

✉ O. Guellati
guellati23@yahoo.fr

[1] LEREC Laboratory, Physics Department, Badji Mokhtar University of Annaba, BP. 12, 23000 Annaba, Algeria

[2] Mohamed Chérif Messaadia University, BP. 1553, 41000 Souk-Ahras, Algeria

[3] Department of Physics, Institute of Applied Materials, SARChI Chair in Carbon Technology and Materials, University of Pretoria, Pretoria 0028, South Africa

Published online: 13 September 2020

Graphic abstract

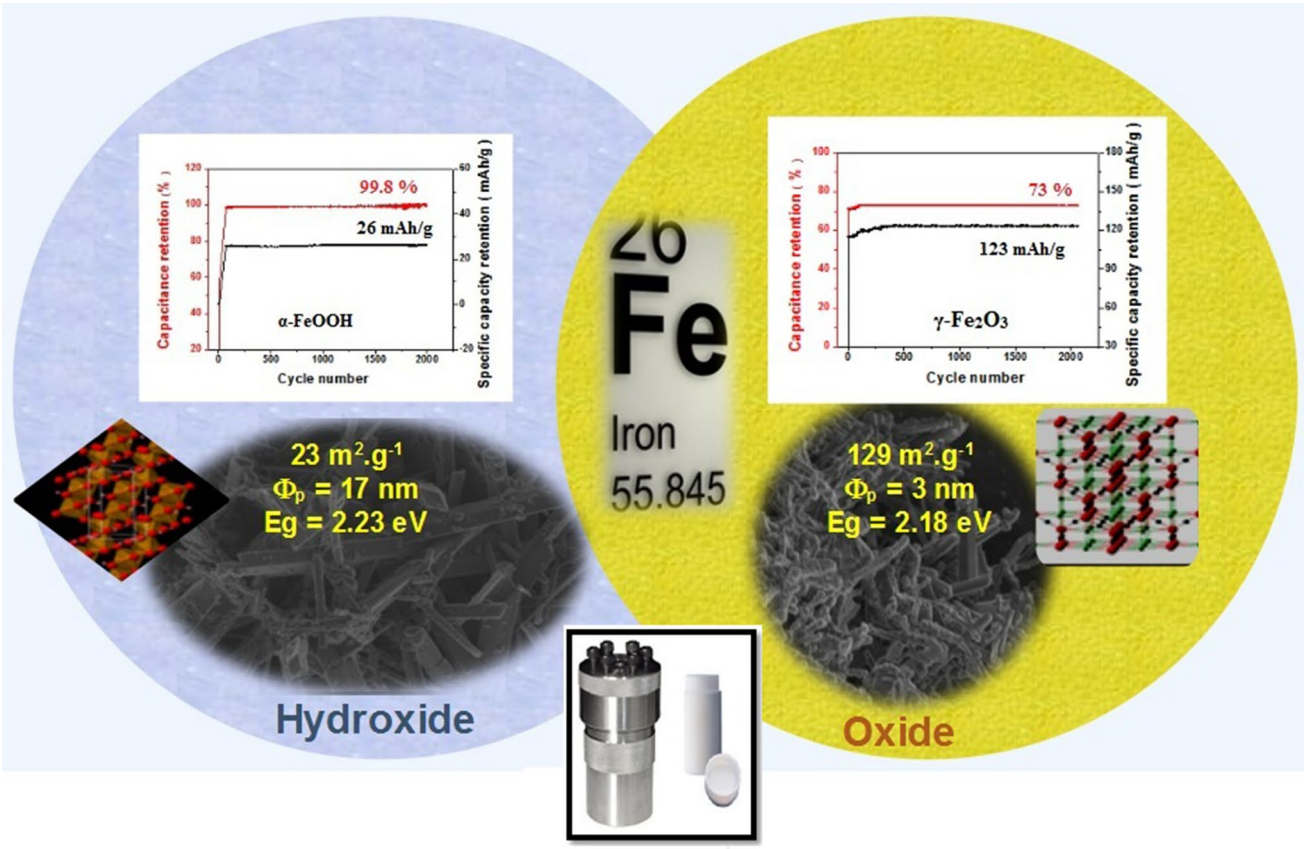

Keywords Hydrothermal synthesis · Iron oxide and hydroxide · Nanofibers · Electrochemical supercapacitors · Energy storage

Introduction

Electrochemical properties of nanostructured materials strongly depend on the nature of the morphology, crystallinity as well as porosity and pore size distribution. Metal-based nanofiber materials are attractive for electrochemical energy-storage applications due to their inexpensive synthesis route, efficient and effective electrochemical stability when used in devices which can satisfy their needs in modern technology [1–3]. Specifically, metal oxides are promising materials in many areas including catalysis, biotechnology, optical and energy-storage devices [4–10].

One of the major merits of adopting metal-based nanostructured materials in supercapacitors (SCs) is the ability to simultaneously store energy via ion adsorption and fast surface redox reactions [11, 12]. Due to this reason, they have received great attention from stakeholders in both academic and industry. Furthermore, they have the ability to deliver characteristic high specific power, quick charging/discharging rates, long cycling life and low maintenance cost in comparison to the conventional capacitors and batteries [13].

Principally, transition metal oxides based on Ni, Mn, Fe or Co, with variable oxidation states, have been studied as attractive electroactive materials for Faradaic supercapacitors due to their fast and reversible redox reaction in the surface region [14]. In particular, iron oxides/hydroxides have shown some remarkable properties in many research fields due to their environmental friendliness, safety, low-cost, natural abundance and relatively high electrical conductivity [2, 15].

It is well known that iron oxides exists in several phases as a result of the variable oxidation states of iron, including iron oxide (FeO, Fe_3O_4, Fe_2O_3) and hydroxide or oxy-hydroxide ($Fe(OH)_2$, $Fe(OH)_3$ and FeOOH) [12, 16–19]. Notably, α-Fe_2O_3 (hematite) is the most thermodynamically stable phase and other phases can be converted to the hexagonal α-Fe_2O_3 by subjecting to some form of heat or pressure treatment [2, 20–23]. Similarly, γ-Fe_2O_3 and Fe_3O_4 (magnetite) also possess a cubic crystal structure of an inverse spinel

type, where Fe^{3+} ions occupy both octahedral and tetrahedral sites and Fe^{2+} ions only occupy the octahedral sites [2].

On the other hand, FeOOH can be found in different crystal structures, like goethite (α-FeOOH), which is the most stable phase and exhibits an orthorhombic crystal structure [19, 24]. It can be obtained by the hydrolysis of iron salts, and it can be transformed to Fe_2O_3 or Fe_3O_4 by heating in air or in an inert gas atmosphere [15, 20–23]. Recent studies have also shown that goethite nanocrystals provide a significant electrochemical capacity in rechargeable Li-ion batteries [25, 26]. Consequently, iron oxide (FeOx) is easily synthesized with different morphologies providing the potential for $Fe^{2+} \leftrightarrow Fe^{3+}$ surface for redox reactions in an aqueous electrolyte. However, various kinds of iron oxides (Fe_3O_4, Fe_2O_3, FeOOH) have been relatively neglected in the literature as potential electroactive materials for supercapacitors because of their inherent high electrical resistance and apparent low cyclability. Recent studies have shown that iron oxides/hydroxides have the potential to emerge as promising class for anode materials for asymmetric supercapacitors [1, 2, 27] although the specific capacitance of the conventional bulk powders is still low, which requires further improvement for the overall energy density of the device [2]. Yang and Wang prepared α-FeOOH@MnO_2 with a specific capacitance of 118.2 F g^{-1} with a retention of about 90% after 3000 cycles [28], while γ-Fe_2O_3/graphene nanocomposite synthesized by Chen and Wang has provided a specific capacitance of about 500 F g^{-1} [29].

Additionally, the synthesis methods used in preparing the nanostructured iron oxide/hydroxide is crucial as it affects the composition and morphology of the final nanostructured material. Different methods, such as sol–gel method [30–32], hydrothermal process [20, 33], co-precipitation [34], high-energy ball milling [35], aerosol pyrolysis [36] and electrochemical synthesis [37] as well as the external influences [38], have been extensively explored. Among all these techniques, the hydrothermal route offers operational simplicity coupled with a relatively low-cost process and environmentally friendly merit as an effective route to control the size and the shape of the obtained nanocrystals. Most studies on hydrothermal synthesis route have been seen to solely focus on two principal parameters which include the growth temperature and vapor pressure [20, 31, 39].

Limited studies have considered a systematic investigation in understanding the combined effect of the growth temperature on the structural, morphological, optical and electrochemical properties of the iron oxide/hydroxide using a basic template-free hydrothermal process. Thus, the novelty and focus of this study is based on the synthesis of two kinds of high-purity iron oxide (γ-Fe_2O_3 and α-FeOOH) nanofibers using a template-free hydrothermal process. The temperature effect was further studied to elucidate the phase transformation of the Fe-based nanofiber. The variation of this synthesis parameter will provide an insight into improving their individual material properties making them potential electrode materials for energy-storage devices.

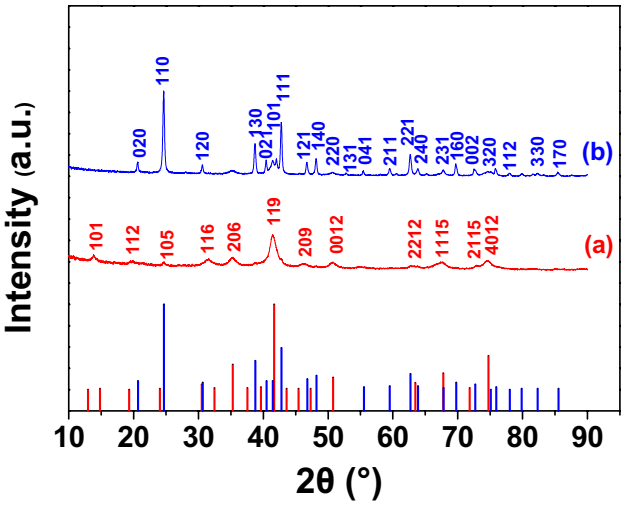

Fig. 1 XRD patterns of iron-based oxide and hydroxide obtained at optimized hydrothermal condition: **a** 130 °C and **b** 200 °C during 3 h growth duration

Experimental procedure

Synthesis of iron oxide and hydroxide-based nanostructures

Iron oxide and hydroxide nanostructure synthesis was carried out using a facile and low-cost template-free hydrothermal process. 0.4 M of ferrous chloride ($FeCl_2 \cdot 4H_2O$) was first dispersed in 25 ml of de-ionized (DI) water. This solution was stirred by adding 3 ml of 12 M NaOH and the suspension was vigorously stirred continuously for 15 min. Subsequently, the obtained brown mixture solution was placed into a 40-ml Teflon-sealed stainless steel autoclave and heated at two different temperatures of 130 °C and 200 °C for a period of 3 h and 18 h (Figure S1). However, further studies only focused on the 3 h synthesis time as initial morphological characterization done on the Fe-based nanofibers showed an undesirable re-agglomeration of these nanorods (Figure S2). Finally, the black product obtained was filtered, washed and rinsed several times with ethanol and DI water before being dried at 80 °C in an electric oven for 20 h.

Table 1 Calculated lattice parameters of the synthesized iron oxide and hydroxide nanostructures

Structure	Lattice parameters		
	a (Å)	*b* (Å)	*c* (Å)
γ-Fe_2O_3 oxide tetragonal [25-1402]	8.51 (8.34)	–	25.10 (25.02)
α-FeOOH hydroxide Orthorhombic [29-0713]	4.67 (4.608)	9.94 (9.956)	3.02 (3.021)

Electrode preparation

The working electrodes were prepared using nickel foam (NiF) current collectors by coating the synthesized electroactive products (Fe_2O_3 or FeOOH with and/or without adding conductive porous activated carbon "AC"). The process involved coating pre-weighed 1 cm × 1 cm area of NiF template with a paste containing 80 wt% active materials, 10 wt% carbon black and 10 wt% polyvinylidene di-fluoride (PVdF). The obtained mass per area of the working electrodes was approximately between 1 and 1.5 mg cm^{-2}.

Characterization techniques

X-ray diffraction (XRD) patterns were obtained from an X' Pert PRO diffractometer (PANalytical BV, Netherlands) operating from a Co-Kα ($\lambda = 1.79$ Å) anti-cathode source.

Raman spectra of the samples were obtained on a JobinYvon Horiba TX 6400 micro-Raman spectrometer excited with the 514 nm line of an argon laser. The laser was set at a power of 1.5 mW and the spectrometer was equipped with a triple monochromator system to eliminate Rayleigh lines contributions. The surface morphology micrographs of the samples were obtained from a Zeiss Ultra Plus 55 field emission scanning electron microscope (FE-SEM) system at 1 kV accelerating voltage. Prior to all analyses, all samples were coated with a thin carbon layer to improve the sample conductivity and their charging effects. However, high-resolution transmission electron microscopy (HR-TEM) images were obtained from a JEOL JEM-2100F microscope operated at 200 kV (Akishima-shi, Japan). The evaluation of the textural properties of the materials was performed on a Tristar II (Micromeritics, 3020) system. The specific surface area (SA) and the pore size distribution analyses were obtained using the Brunauer–Emmett–Teller (BET) and Barrett–Joyner–Halenda (BJH) models, respectively. All samples were initially de-gassed for 18 h under vacuum at room temperature to avoid material transformation but allowing the removal of sample impurities and surface moisture. The optical properties were carried out by measuring the absorbance using a UV–Vis spectrophotometer (Thermo Technical GENESYS 10S) with double beam to examine the energy bandgap of our products. The measurements were obtained from nanoparticles dispersed in DI water at the wavelength range from 190 to 1100 nm.

All electrochemical measurements were performed using a Gamry Instrument (REF 600^{TM}Potentiostat/Galvanostat/ZRA) with a three-electrode experimental cell in 6 M KOH aqueous electrolyte using a Hg/HgO reference electrode and Pt counter electrode. Cyclic voltammetry (CV) and galvanostatic charge–discharge (GCD) tests were done from 0 to 0.6 V (vs. Hg/HgO) potential at increasing scan rates (5–100 Mv s^{-1}) and gravimetric currents (1–100 A g^{-1}), respectively. Electrochemical impedance spectroscopy (EIS) test was performed in frequencies ranging from 0.1 Hz to 100 kHz on open circuit potential.

The specific capacity 'Q_s in mAh g^{-1}' can be obtained from the GCD curve according to Eq. (1) [40]:

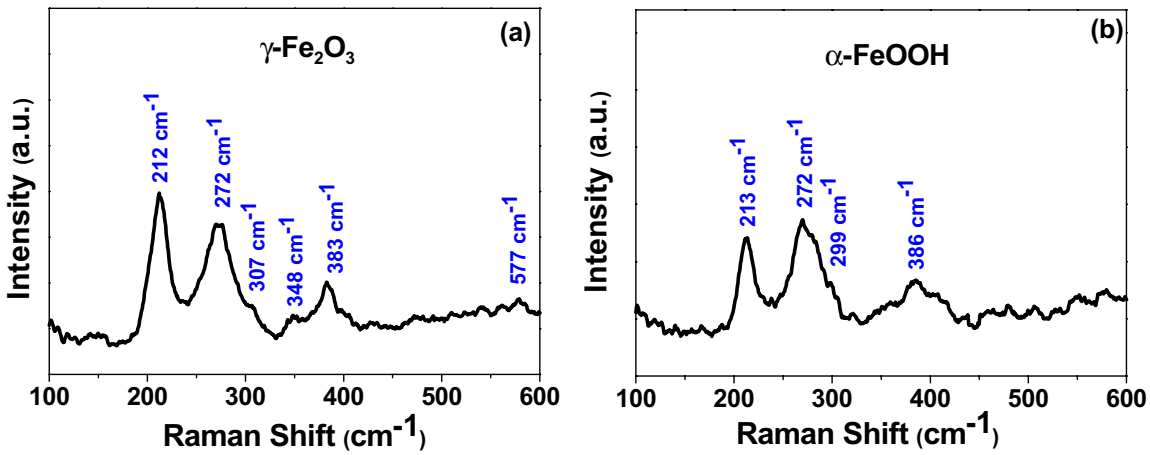

Fig. 2 Raman spectra of the obtained iron oxide and hydroxide nanostructures at two different growth temperatures during 3 h: **a** 130 °C and **b** 200 °C

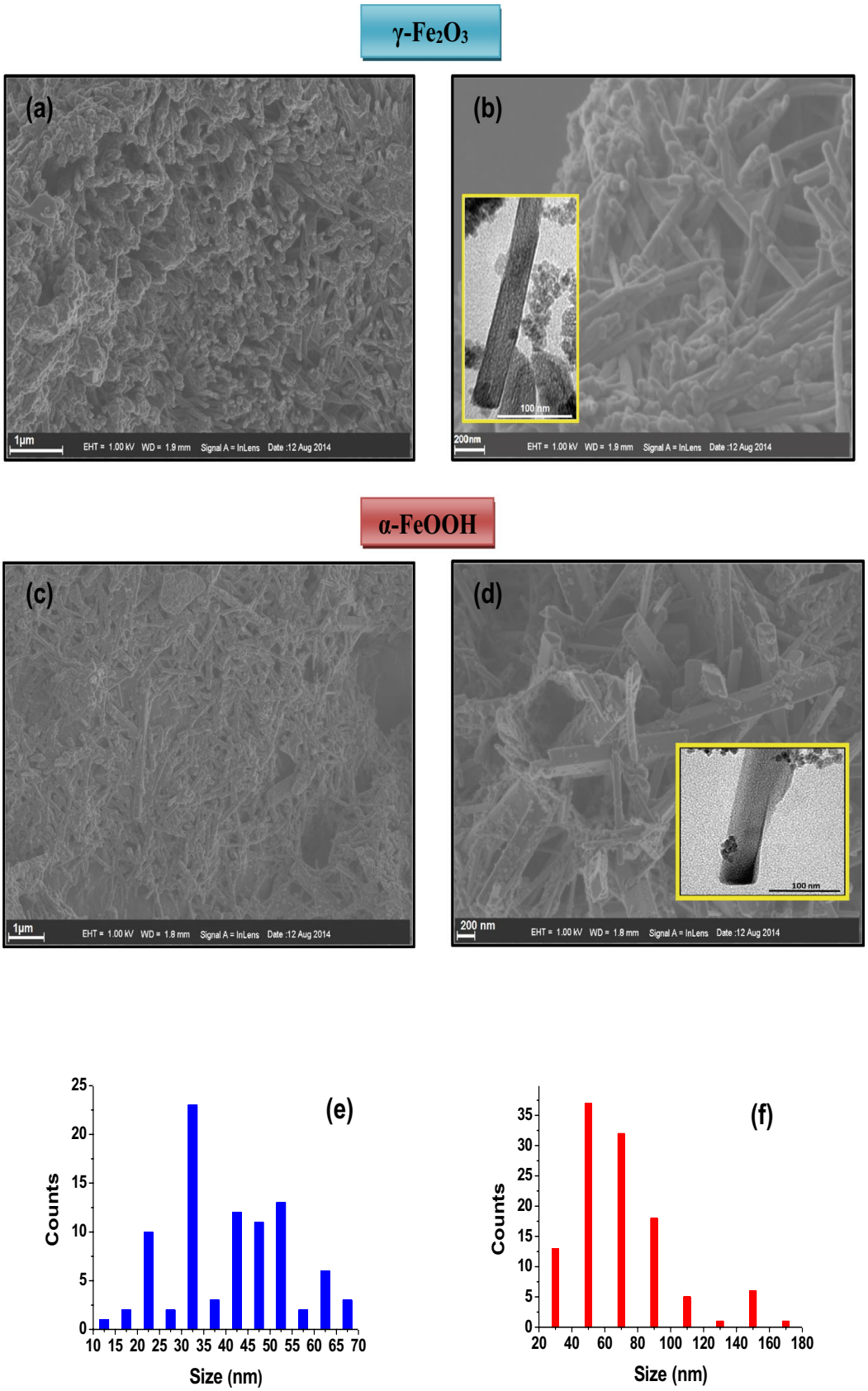

Fig. 3 FESEM micrographs of iron-based oxide nanorods (**a**, **b**) grown at 130 °C; iron-based hydroxide nanotrigonals (**c**, **d**) grown at 200 °C; inset to **b**, **d** shows the HRTEM micrographs; **e**, **f** their histograms

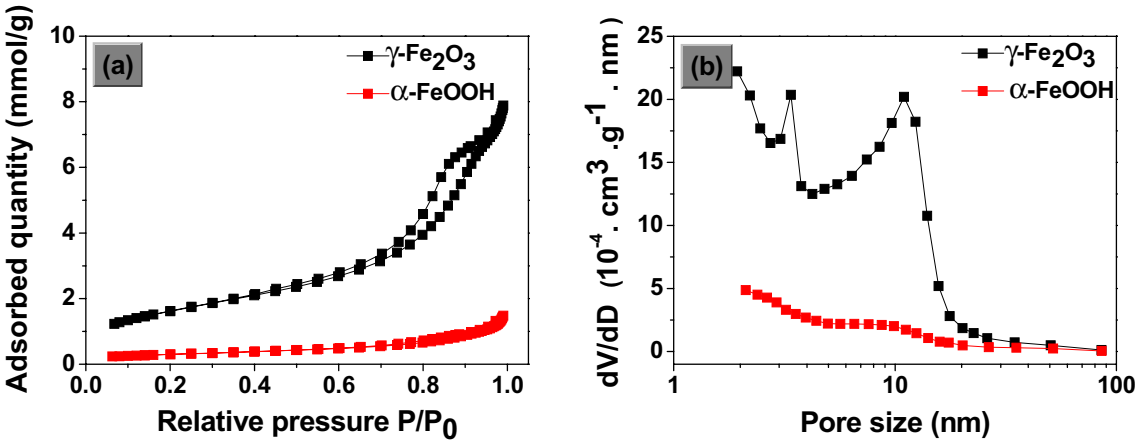

Fig. 4 N_2 adsorption–desorption isotherms (**a**) and BJH desorption d*V*/d*D* pore volume (**b**) of the iron oxide and hydroxide products

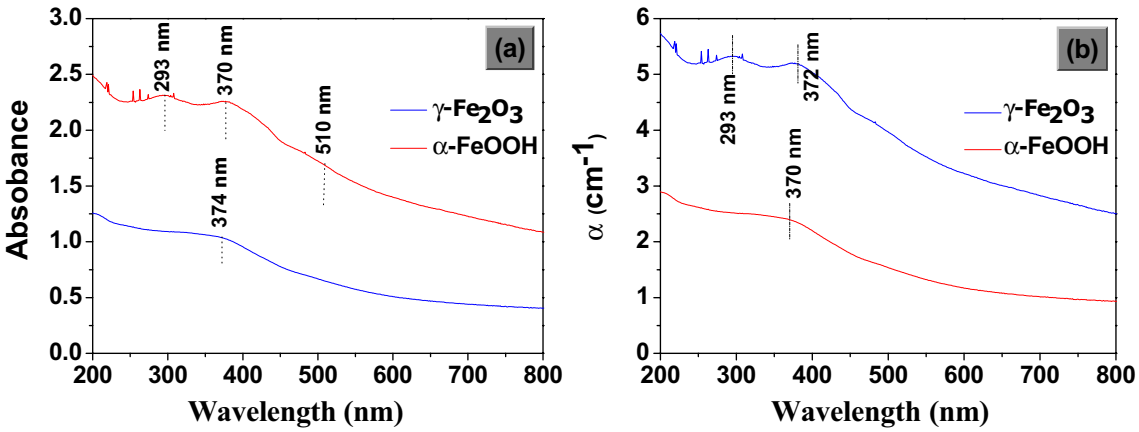

Fig. 5 **a** UV–Vis absorbance spectra and **b** absorbance coefficient for the γ-Fe_2O_3 and α-FeOOH nanofibers

$$Q_s = \frac{i\Delta t}{3.6}, \tag{1}$$

where $i = \frac{I}{m}$ is the gravimetric current and Δt is the discharge time. m is the electroactive material weight (g) without the current collector.

Results and discussion

Structural and morphological properties

The XRD patterns of the as-synthesized iron oxide and iron hydroxide samples with optimized hydrothermal growth conditions are presented in Fig. 1. The formation of γ-Fe_2O_3 and α-FeOOH at two different growth temperatures of 130 °C and 200 °C is clearly observed as the following reaction mechanism:

For the γ-Fe_2O_3 at 130 °C:

$$4FeCl_2 + 8NaOH + O_2 \rightarrow 2Fe_2O_3 + 8NaCl + 4H_2O. \tag{2}$$

When the reaction temperature increased from 130 to 200 °C, we obtained an α-FeOOH nanomaterial in two steps as follows:

$$FeCl_2 + 2NaOH \rightarrow Fe(OH)_2 + 2NaCl. \tag{3}$$

$$Fe(OH)_2 + O_2 \rightarrow FeOOH + H_2O. \tag{4}$$

Figure 1a shows single-phase γ-Fe_2O_3 oxide formation according to the obtained peaks at 41° (119), 35° (206), 50° (0012) and 74° (402) which are assigned to a tetragonal structure depending to the standard JCPDS card no. 25-1402.

However, Fig. 1b shows the formation of the α-FeOOH hydroxide phase according to the pure orthorhombic structure peaks found at 24° (110), 38° (012), 42° (111) and 62° (221) depending to the standard JCPDS card no. 29-0713.

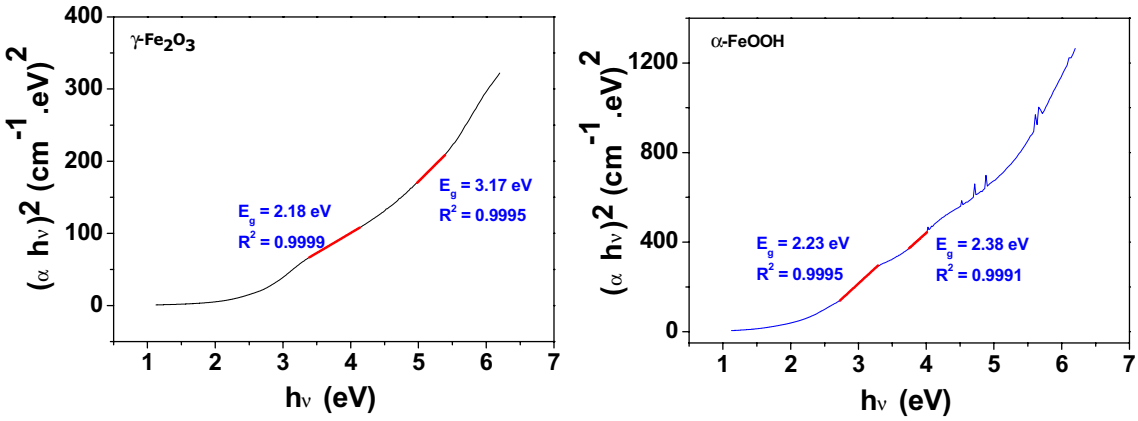

Fig. 6 The Tauc's plots of $(\alpha h\nu)^2$ versus photon energy $(h\nu)$ for γ-Fe_2O_3 and α-FeOOH nanofibers

The fitting results for lattice parameters are summarized in Table 1; which is in agreement with their JCPDS reference cards [15, 28, 41].

The iron oxide (γ-Fe_2O_3) and hydroxide (α-FeOOH) samples were also analyzed using Raman spectroscopy (see Fig. 2). Figure 2a displays the Raman spectrum of the γ-Fe_2O_3 nanomaterial with the distinct broad bands around 212, 272, 350, 380, and 570 cm^{-1} [42, 43]. Figure 2b shows three quasi-broad bands at 212, 271 and 383 cm^{-1} [24]; the first two wavenumbers are linked to the hematite structure while the peak around 386 cm^{-1} is attributed to the E_{1g} symmetrical stretching mode for Fe–O–Fe/–OH band in the same direction. These are in agreement with similar reports from earlier studies [44, 45].

The morphology and the size distribution homogeneity of the as-obtained nanostructured products were also examined by FESEM and HRTEM techniques as shown in Fig. 3. The micrographs (at high and low magnification) clearly show nanofibers formation with circular bases (nanorods) for γ-Fe_2O_3 having a diameter of ~ 32 nm and a 300 nm length (Fig. 3a, b). However, when the growth temperature increases (from 130 to 200 °C), the structural phase and the morphology change to α-FeOOH with regular trigonal nanofibers having ~ 50 nm diameter and 500 nm length (Fig. 3c, d). These latter morphologies have been confirmed through HRTEM images shown in the inset figure where trigonal edge-based nanofibers, for example, were clearly illustrated. In addition, for the nanofiber, size distribution is shown in histograms which are presented in Fig. 3e, f. The results clearly prove that the hydrothermal growth temperature has a significant effect on the products morphological and structural properties.

In general, specific surface area (SSA), pore diameter and pore volume of any material play also an important role in materials' electrochemical performance. Therefore, the porous nature of our iron oxide and hydroxide nanofibers was investigated using nitrogen physisorption analysis. The adsorption–desorption isotherms of the as-synthesized products were of type IV with a hysteresis loop recorded at a relative pressure (P/P_0) between 0.7 and 1 characterizing the mesoporous textural products as exhibited in Fig. 4 [40, 46].

BET SSA values of 129 $m^2\ g^{-1}$ and 23 $m^2\ g^{-1}$ were obtained for the iron oxides (γ-Fe_2O_3) and hydroxides (α-FeOOH), respectively. The Barrett–Joyner–Halenda (BJH) pore size distribution curves confirmed the formation of a mesoporous material with maximum pore diameters between 3 and 17 nm (< 50 nm) and associated pore volumes of approximately 0.28 $cm^3\ g^{-1}$ and 0.1 $cm^3\ g^{-1}$, respectively. Thus, the relatively high SSA and pore volume of the γ-Fe_2O_3 nanorods provides the possibility for efficient ions transport, leading to high electrochemical capacity [47]. The textural mesoporosity of the nanofibers aids the feasible movement of ions as active charge storage sites for electrochemical reactions at higher current density [48].

Furthermore, in comparison with the FESEM and HRTEM analysis results, it is likely that the high specific surface area recorded for the iron oxide nanorods is due to its smaller sized cross section (32 nm) and the arrangement in the products in comparison with hydroxides (50 nm).

Optical properties

Optical absorption and electronic structure of the synthesized iron oxide-based nanofibers were estimated using UV–visible absorption spectroscopy as shown in Fig. 5, which depicts the absorbance spectrum as a function of wavelength for the iron oxide and hydroxide nanofibers in the range of 190–1100 nm giving the existing electronic transition. This figure shows clearly the difference in the absorbance degree of both Fe-based nanofibers. Generally, three kinds of electronic transition occur in the process of light absorption; from Fe^{3+} ligand to metal charge

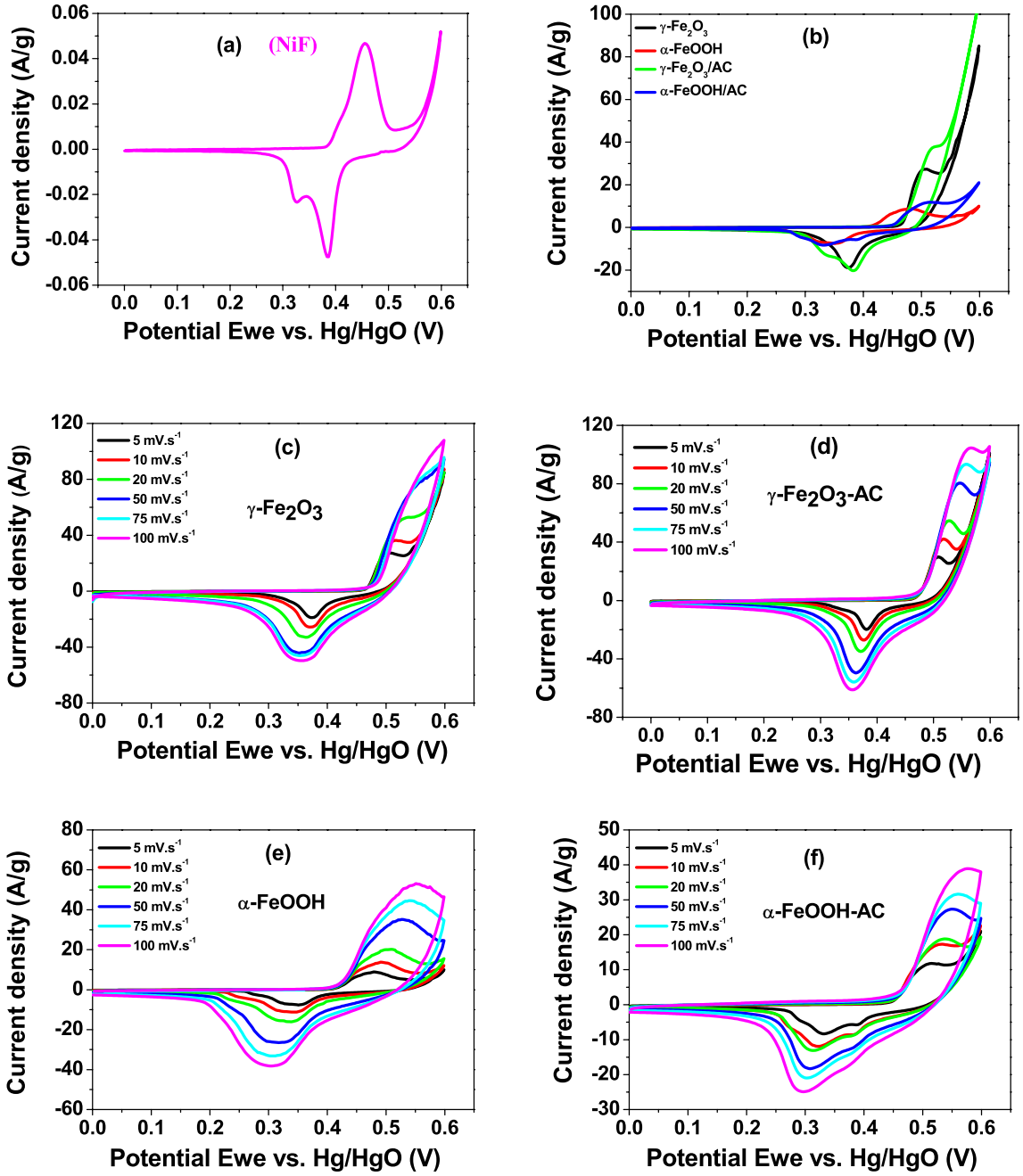

Fig. 7 CV curves of **a** NiF bare without electroactive material, **b** comparison between γ-Fe_2O_3 and α-FeOOH with and without AC addition at 5 mV s^{-1} scan rate, **c**–**f** for all products at varying scan rates

transfer (250–400 nm) along with contribution of Fe^{3+} ligand field transition (290–310 nm), pair excitation process (400–600 nm) of magnetically coupled Fe^{3+} ions [21, 49]. In our case from these results, three-strip broad absorption band of α-FeOOH nanofibers are mainly located in an area away from UV.

One of these bands is a ligand to metal charge transfer located in the wavelength range of 290–310 nm and the second region in the 360–380 nm range is linked to the contribution of Fe^{3+} ligand field transition. The obtained peaks at 290 and 370 nm correspond to the transition of a pure goethite structure [50]. For γ-Fe_2O_3, the absorbance curve shows a band at around 370 nm, as saturated band below 400 nm which is due to a paired Fe^{3+}–O^{-2} charge transfer as reported by previous studies [51].

The optical energy bandgap (E_g) is one of the important electrical parameters. In general, it is the minimal energy of an absorbed photon to generate free electron–hole couple

Table 2 Comparison of the specific capacity and cycling performance depending on the synthesis method, the electrolyte and the electroactive material morphology

Products	Synthesis method	Morphology	Electrolyte	Cs (mAh g^{-1})	Cycling performance	References
γ-Fe_2O_3 α-FeOOH	Hydrothermal	Nanofibers	KOH	330 69	73% 99.8% (2000 cycles)	Our results
Fe_3O_4/AC	Precipitation	Nanocomposite	KOH	247	93% (1000 cycles)	[58]
CC-CNT@Fe_2O_3	Aqueous reduction	Nanocomposite	KOH	226	–	[59]
K-FeOOH/Fe_3O_4/SS	Hydrothermal		KOH	396	–	[60]
3D Fe_2O_3/Fe_3O_4	In situ chemical reaction		LiPF6	797.9	–	[58]
γ-Fe_2O_3	Solvothermal	Microspheres	LiPF6	201	93% (1000 cycles)	[61]
PANI/α-Fe_2O_3		Nanocomposite	H_2SO_4	29 F/g	94%	[62]
$CoFe_2O_4$	Hydrothermal	Spinel NPs	KOH	442	98% (6000 cycles)	[55]
FeOOH@MnO_2	Solution approach	Core–shell	KOH	178	90% (3000 cycles)	[23]

in conductance and valence bands. The optical E_g can be determined through the Tauc–Mott (TM) plot and the relationship between the absorption coefficient and the incident photon energy experimentally was obtained using Tauc's formula [21, 51, 52]:

$$(\alpha h\nu)^n = A(h\nu - E_g), \tag{5}$$

where α is the absorption coefficient, A is a constant and n is a constant depending to the transition nature of the energy bandgap (n equals to 2 and 0.5 for direct and indirect transitions, respectively) [53]. The optical bandgap values are obtained by extrapolating the linear portion of the curves plotted between $(\alpha h\nu)^2$ and $(h\nu)$, to intersect X-axis. The estimated values of E_g from Fig. 6 are 2.18 and 2.23 eV for γ-Fe_2O_3 and α-FeOOH, respectively. It can be noticed that this E_g energy was found to be increased with increasing the temperature growth, which can be associated with the structural composition and crystallite size. These obtained values are almost similar to those reported in other related studies in the literature [21, 50].

Electrochemical properties

Cyclic voltammetry (CV) tests are used to study the energy-storage mechanism of our synthesized iron oxide and hydroxide-based nanofibers via a template-free hydrothermal method. For faradic-type materials (transition metal oxides and hydroxides), the presence of redox peaks provide relevant electrochemical (EC) information, such as electron transfer kinetics and adsorption process in relation to the redox process thermodynamics [14].

Figure 7 displays the obtained CV curves of the iron oxide (γ-Fe_2O_3) and hydroxide (α-FeOOH) nanofibers at different scan rates with and without AC addition in the potential range from 0 to 0.6 V (vs. Hg/HgO). These curve shapes indicate clearly that our synthesized electroactive nanofibers have faradic redox behavior through pair of redox peaks observed at around 0.5 V and 0.35 V which correspond to possible change of oxidation state between Fe^{2+} and Fe^{3+} [54]. It is also noted that the peak currents of these CV curves increase with increasing scan rates which is in accordance with previous electrochemical investigations [40, 55]. In addition, the reduction and the oxidation peaks undergo evident shifts with a potential separation between these peaks [56].

Furthermore, the area under these CV curves is clearly much larger in the case of iron oxide (γ-Fe_2O_3) in comparison to those of hydroxide (α-FeOOH) (Fig. 7b) in both cases with and without AC addition. This depicts the ability of the γ-Fe_2O_3 to store more charge as compared to the α-FeOOH [57]. The influence of the NiF template on the electrochemical performance is negligible which is shown in Fig. 7a.

Table 2 presents a comparison of the electrochemical performance of different Fe-based nanomaterials with the charge storage ability of our synthesized nanofibers. The results obtained in the current study confirm the importance of carefully selecting the synthesis temperature in relation to the specific phase of the Fe-based nanomaterial. In addition, the novelty of our results lies once again in using a facile template-free hydrothermal method in aqueous electrolytes.

Figure 8a shows the plots of peak current (I_p) for both anode and cathode versus square root of scan rate ($\nu^{1/2}$). A linear relationship is obtained which reveals and confirms that these faradic reactions are controlled by proton diffusion which is in agreement with previous works in the literature [40]. However, Fig. 8b shows the relationship between the change in peak potentials difference, ΔE_p ($E_{pa} - E_{pc}$) and the scan rate (ν). We found that most ΔE_p values are less than 200 mV at further lower scan rate ($\nu < 50$ mV s^{-1}) in

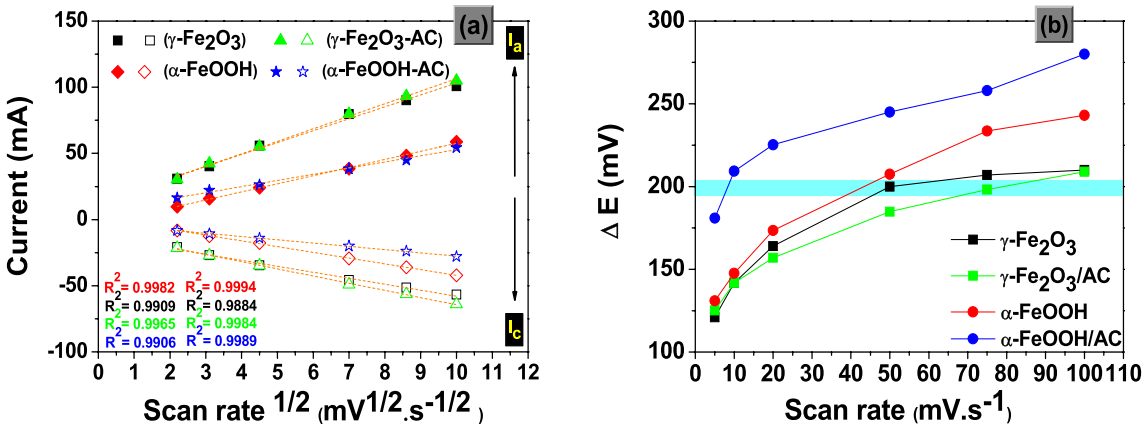

Fig. 8 Relationship between: **a** I_p versus $v^{1/2}$ and **b** ΔE versus ν

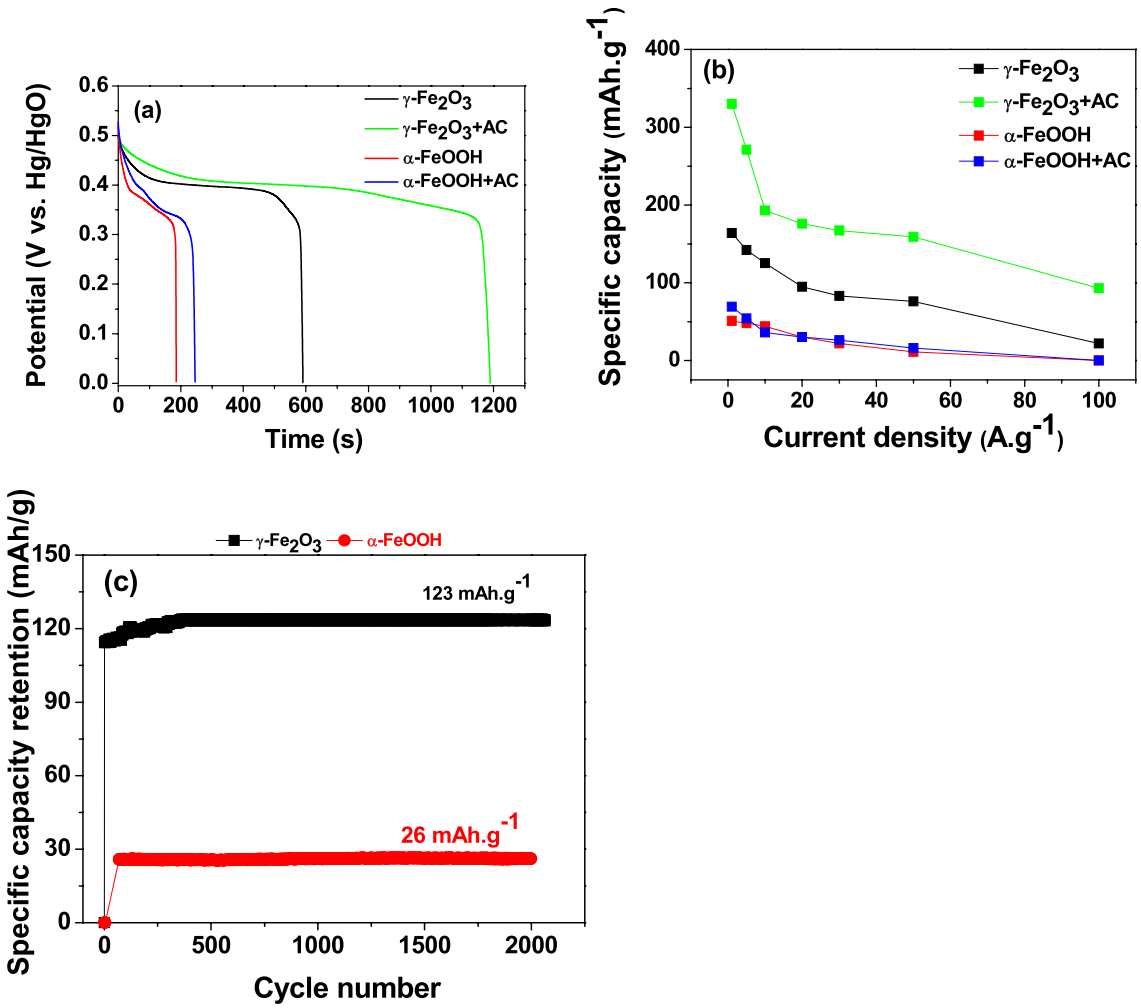

Fig. 9 **a** GCD curves at 1 A g^{-1} current density, **b** specific capacity via current density for iron oxide and hydroxide with and without AC, **c** specific capacity retention as a function of cycling for both γ-Fe_2O_3 and α-FeOOH nanofibers at 30 A g^{-1}

all products thus confirming the reversibility of the redox phenomena kinetic as reported in earlier studies [63].

The galvanostatic charge/discharge (GCD) tests for the γ-Fe_2O_3 and α-FeOOH electroactive nanofibers with and without AC at 1 A g^{-1} in a potential range [0–0.6 V] are shown in Fig. 9a. The shape of these obtained curves also confirms the presence of a Faradic-type charge storage mechanism and thus the corresponding specific capacities

are calculated. Figure 9b shows the specific capacity as a function of gravimetric current density with the γ-Fe_2O_3 nanorods exhibiting a better specific capacity ~ 164 mAh g^{-1} as compared to α-FeOOH trigonal nanofibers (51 mAh g^{-1}). An evident gradual decrease in specific capacity with increasing gravimetric current density confirms a diffusion limitation of the electrolyte ions due to insufficient interaction time with active sites within the nanofibers [40, 64, 65]. Thus, only the outer active surfaces of these iron-based nanofibers are used for charge storage at fast charge–discharge rates [66]. The observed improvements in charge storage capability in the oxide material is linked to the higher specific surface area values of γ-Fe_2O_3 which is five times higher than that of α-FeOOH. These pore sites act as ion-buffering reservoirs and transport channels for efficient charge storage. Furthermore, the favorable structural and morphological characteristics of the synthesized iron-based nanofibers contribute to minimizing the diffusion distance which may accelerate the kinetic process of the ion diffusion in the electrode to interior surfaces. They also allow rapid ion and electron transportation process, which leads to the exhibited higher electrochemical performance [48, 67].

Figure 9c shows the cyclic stability of our both γ-Fe_2O_3 and α-FeOOH nanofibers from the capacity retention as a function of cycle number at 30 A g^{-1} current density for up to 2000 charge–discharge cycles. In the case of γ-Fe_2O_3-based electroactive material, a 73% capacity retention was recorded corresponding to a discharge capacitance of ca. 123 mAh g^{-1}. However, for the α-FeOOH electroactive material, a high capacity retention around 99.8% was obtained but with a relatively lower capacity retention of about 26 mAh g^{-1}. Thus, these results confirm exactly our previous investigation.

EIS measurements were carried out to further evaluate the electrochemical behavior of the synthesized mesoporous nanofiber material electrodes. Figure 10 presents the Nyquist plots obtained for our products which prove that the γ-Fe_2O_3 nanofibers show best product before and after their cycling test with and without AC.

A semi-circular arc in the high-frequency region accompanied with a slightly inclined vertical line in the

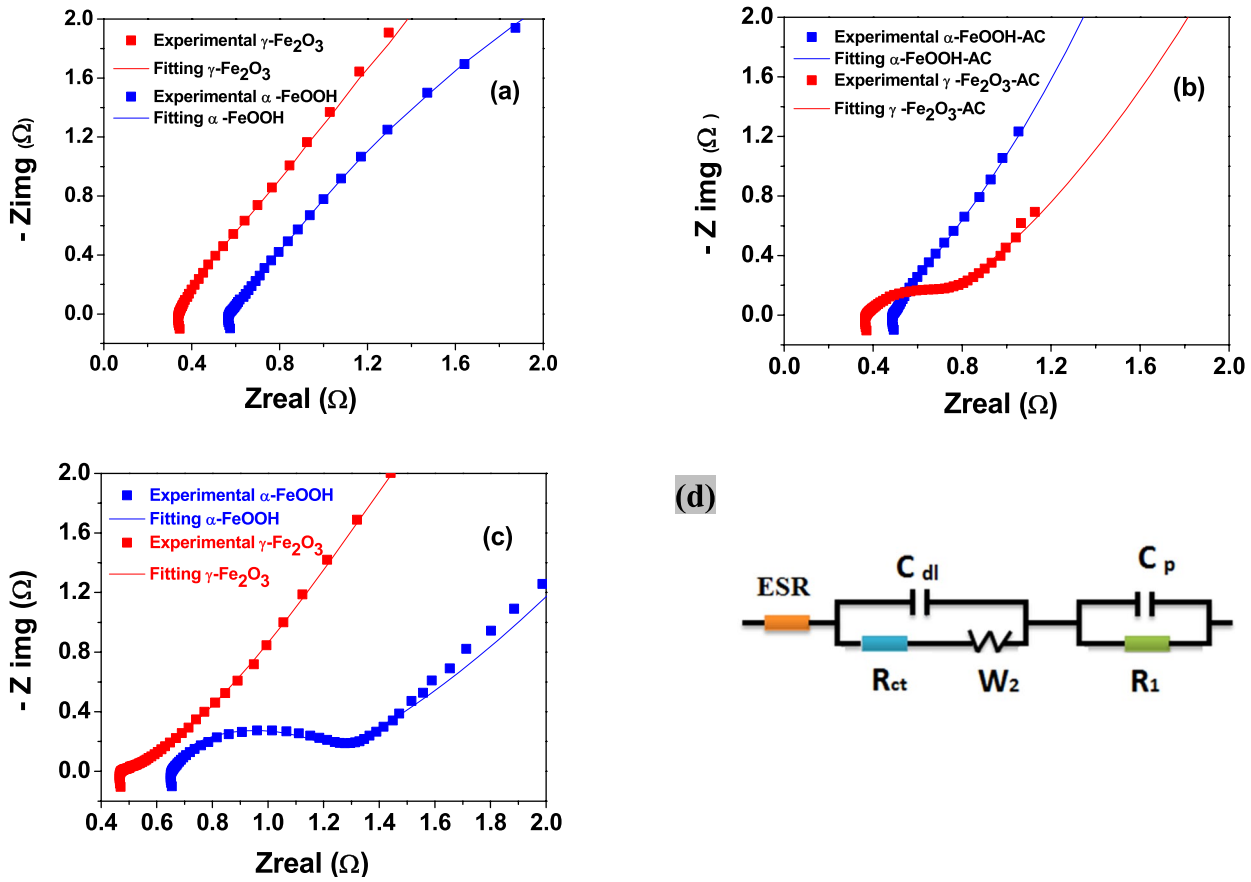

Fig. 10 **a**, **b** Nyquist plots for γ-Fe_2O_3, α-FeOOH with and without AC, **c** for γ-Fe_2O_3, α-FeOOH after cycling, **d** their equivalent circuit

low-frequency region is observed. The charge transfer kinetic normally occurs at intermediate to high-frequency range, whereas ionic diffusion (mass transfer) takes place in the low-frequency range [29, 40, 68]. More so, to explain the individual processes and associated impedance parameters, an equivalent circuit of our EIS measurements containing a combination of equivalent series resistance (ESR), electrical double-layer capacitance (C_{dl}), charge transfer impedance (R_{ct}), a frequency-dependent Warburg resistance (W), pseudocapacitance (C_p) and leakage resistance (R_1) has been modeled [28, 29, 40, 68] and shown in Fig. 10d.

Therefore, the obtained EIS data have been fitted according to the proposed equivalent circuit shown in Fig. 10d which was depicted at the high-frequency region by the intercept at real part of the impedance axis (Z_{real}). The series resistance (R_s) is a combinational resistance of electrolyte ionic resistance, current collector intrinsic resistance and interface contact resistance between the electroactive nanofibers and the current collector [40]. Also, the semi-circular curve could be seen, whose diameter represents the charge transfer resistance (R_{ct}) caused by the faradic phenomena on the grain surface and a straight inclined line in the lower frequency region which represents the Warburg element (W) linked to the semi-infinite diffusion transport of counter ions between the KOH electrolyte and the electroactive pores during the redox reactions [55]. Therefore, on the basis of these fitted data, the values of R_s and R_{ct} were calculated and are presented in Table 3. These results confirm also that our γ-Fe_2O_3 nanorods showed better electronic transport and lower charge transfer resistance than that of α-FeOOH trigonal nanofibers due to their physico-chemical properties shown previously, which help the diffusion of ions inside the electroactive material.

The R_{ct} value recorded after 2000 cycles was seen to be slightly increased from 0.4 to 0.5 Ω for the γ-Fe_2O_3 material electrode and 0.64 to 1.3 Ω for α-FeOOH electrode. This is possibly due to the loss of some active material adhesion with the NiF current collector or the dissolution of these oxides during the charge/discharge cycling [28, 69]. On the other hand, it is observed that the AC addition to the electroactive synthesized materials improved more their conductivity.

Table 3 Fitting parameters of equivalent circuit for iron oxide and hydroxide before and (*) after cycling

Electrode	R_s (Ω)	R_{ct} (Ω)
γ-Fe_2O_3	0.32 (0.47*)	0.4 (0.5*)
α-FeOOH	0.57 (0.67*)	0.64 (1.3*)
γ-Fe_2O_3/AC	0.37	0.4
α-FeOOH/AC	0.49	0.53

Conclusion

In this study, the as-synthesized γ-Fe_2O_3 and α-FeOOH nanofibers with different morphology (nanorods and trigonal nanofibers, respectively) were shown with interesting optical and electrochemical performances. Precisely, the γ-Fe_2O_3 nanofibers present better electrochemical properties compared to those of α-FeOOH hydroxide due to their effective mesoporous textural character with high specific surface area and pore volume (129 $m^2\ g^{-1}$/0.28 $cm^3\ g^{-1}$, respectively) which makes them more attractive as electrode materials for energy-storage devices.

Furthermore, comparing a pure γ-Fe_2O_3, α-FeOOH and their mixture with AC conductive additives, we found that the γ-Fe_2O_3/AC mixture possessed a higher specific capacity of ~ 330 mAh g^{-1}, which opens a new pathway to the development of high-performance supercapacitors due to their good stability, fast ion transport and diffusion rate in alkaline aqueous electrolytes.

Consequently, the present work offers simple, effective template-free synthesis approach in producing novel iron-oxide-based nanofibers with interesting optical and electrochemical properties. Further work is still on going to adopt the results obtained from the optical characterization for optoelectronic device applications.

Acknowledgements The present work is based on the research supported by the Algeria and South Africa collaboration program between LEREC laboratory, Badji Mokhtar-Annaba University and South African Research Chairs Initiative (SARChI) in Carbon Technology and Materials of the Department of Science and Technology project number 61056. The financial support received from National Research Foundation (NRF) from Pretoria and Directorate General for Scientific Research and Technological Development (DGRSDT) from Algeria.

Compliance with ethical standards

Conflict of interest The authors declare that there is no conflict of interest.

References

1. An, C., Zhang, Y., Guo, H., Wang, Y.: Metal oxide-based supercapacitors: progress and prospectives. Nanoscale Adv. **1**, 4644–4658 (2019)
2. Xia, Q., Xu, M., Xia, H., Xie, J.: Nanostructured iron oxide/hydroxide based electrode materials for supercapacitors. ChemNanoMat. **2**, 588 (2016)
3. Cao, D., Li, H., Pan, L., Li, J., Jing, P., Cheng, X., Wang, W., Wang, J., Liu, Q.: High saturation magnetization of γ-Fe_2O_3 nano-particles by a facile one-step synthesis approach. Sci. Rep. **6**, 32360 (2016)
4. Doustkhah, E., Lin, J., Rostamnia, S., Len, C., Luque, R., Luo, X., Bando, Y., Wu, K.C.W., Kim, J., Yamauchi, Y., Ide, Y.:

Development of sulfonic-acid-functionalized mesoporous materials: synthesis and catalytic applications. Chem. Eur. J. **24**, 1–23 (2018)
5. Lee, C.C., Chen, C.I., Liao, Y.T., Wu, K.C.W., Chueh, C.C.: Enhancing efficiency and stability of photovoltaic cells by using perovskite/Zr-MOF heterojunction including bilayer and hybrid structures. Adv. Sci. **6**, 1801715 (2019). https://doi.org/10.1002/advs.201801715
6. Chueh, C., Chen, C., Su, Y., Konnerth, H., Gu, Y., Kung, C., Wu, K.C.W.: Harnessing MOF materials in photovoltaic devices: recent advances, challenges, and perspectives. J. Mater. Chem. A **7**, 17079–17095 (2019)
7. Liao, Y.T., Matsagar, B.M., Wu, K.C.W.: Metal-organic frameworks (MOFs) derived effective solid catalysts for the valorization of lignocellulosic biomass. ACS Sustain. Chem. Eng. **6**(11), 13628–13643 (2018)
8. Liao, Y., Chi, N.V., Ishiguro, N., Young, A.P., Tsung, C., Wu, K.C.W.: Engineering a homogeneous alloy-oxide interface derived from metal organic frameworks for selective oxidation of 5-hydroxymethylfurfural to 2, 5-furandicarboxylic acid. Appl. Catal. B Environ. **270**, 118805 (2020)
9. Konnerth, H., Matsagar, B.M., Chen, S.S., Prechtl, M.H.G., Shieh, F.K., Wu, K.C.W.: Metal-organic framework (MOF)-derived catalysts for fine chemical production. Coord. Chem. Rev. **416**, 213319 (2020)
10. Dukenbayev, K., Korolkov, I.V., Tishkevich, D.I., Kozlovskiy, A.L., Trukhanov, S.V., Gorin, Y.G., Shumskaya, E.E., Kaniukov, E.Y., Vinnik, D.A., Zdorovets, M.V., Anisovich, M., Trukhanov, A.V., Tosi, D., Molardi, C.: Fe_3O_4 Nanoparticles for complex targeted delivery and boron neutron capture therapy. Nanomaterials **9**, 494 (2019)
11. Zhao, C., Zheng, W.: A review for aqueous electrochemical supercapacitors. Front. Energy Res. **3**, 23 (2015)
12. Zeng, Y., Yu, M., Meng, Y., Fang, P., Lu, X., Tong, Y.: Iron-based supercapacitor electrodes: advances and challenges. Adv. Energy Mater. **6**, 1601053 (2016)
13. Brousse, T., Crosnier, O., Bélanger, D., Long, J.W.: Metal Oxides in Supercapacitors Metal Oxides, pp. 1–24. Elsevier Inc., Amsterdam (2017)
14. Zhang, G., Xiao, X., Li, B., Gu, P., Xue, H., Pang, H.: Transition metal oxides with one-dimensional/one dimensional analogue nanostructures for advanced supercapacitors. J. Mater. Chem. A **5**, 8155–8186 (2017)
15. Wang, M., Cheng, S., Dang, G., Min, F., Li, H., Zhang, Q., Xie, J.: Solvothermal synthesized γ-Fe_2O_3/graphite composite for supercapacitor. Int. J. Electrochem. Sci. **12**, 6292–6303 (2017)
16. Yue, J., Jiang, X., Kaneti, Y.V., Yu, A.: Deposition of gold nanoparticles on β-FeOOH nanorods for detecting melamine in aqueous solution. J. Colloid Interface Sci. **367**(1), 204–212 (2012)
17. Kozlovskiy, A.L., Ermekova, A.E., Korolkov, I.V., Chudoba, D., Jazdzewska, M., Ludzik, K., Nazarova, A., Marciniak, B., Kontek, R., Shumskayah, A.E., Zdorovets, M.V.: Study of phase transformations, structural, corrosion properties and cytotoxicity of magnetite-based nanoparticles. Vacuum **163**, 236–247 (2019)
18. Wei, Y., Ding, R., Zhang, C., Lv, B., Wang, Y., Chen, C., Wang, X., Xu, J., Yang, Y., Li, Y.: Facile synthesis of self-assembled ultrathin α-FeOOH nanorod/graphene oxide composites for supercapacitors. J. Colloid Interface Sci. **504**, 593–602 (2017)
19. Kasparis, G., Erdocio, S., Tuffnell, J.M., Thanh, N.T.K.: Synthesis of size-tuneable β-FeOOH nanoellipsoids and a study of their morphological and compositional changes by reduction. CrystEngComm **21**, 1293–1301 (2019)
20. Ozel, F., Kockar, H., Karaagac, O.: Growth of iron oxide nanoparticles by hydrothermal process: effect of reaction parameters on the nanoparticle size. J. Supercond. Nov. Magn. **28**, 823–829 (2015)
21. Lee, S.W., Surabhi, S., Kuchi, R., Sohn, Y., Jeong, J.: Magnetic/catalytic properties and strain induced structural phase transformation from β-FeOOH to porous α-Fe_2O_3 nanorods. J. Alloy Compd. **771**, 131–139 (2019)
22. Adhyapak, P.V., Mulik, U.P., Amalnerkar, D.P., Mulla, I.S.: Low temperature synthesis of needle-like α-FeOOH and their conversion into α-Fe_2O_3 nanorods for humidity sensing application. Am. Ceram. Soc. **96**(3), 731–735 (2013)
23. El Mendili, Y., Bardeau, J.F., Randrianantoandro, N., Greneche, J.M., Grasset, F.: Structural behavior of laser-irradiated γ-Fe_2O_3 nanocrystals dispersed in porous silica matrix: γ-Fe_2O_3 to α-Fe_2O_3 phase transition and formation of ε-Fe_2O_3. Sci. Technol. Adv. Mater. **17**(1), 597–609 (2016)
24. Luo, W., Jiang, C., Li, Y., Shevlin, S.A., Han, X., Qiu, K., Cheng, Y., Guo, Z., Huang, W., Tang, J.: Highly-crystallized α-FeOOH for stable and efficient oxygen evolution reaction. J. Mater. Chem. A **5**, 2021–2028 (2017)
25. Fadeev, M., Kozlovskiy, A., Korolkov, I., Egizbek, K., Nazarova, A., Chudoba, D., Rusakov, V., Zdorovets, M.: Iron oxide @ gold nanoparticles: synthesis, properties and potential use as anode materials for lithium-ion batteries. Colloid Surf. A Physicochem. Eng. Asp. **603**, 125178 (2020)
26. Yu, S., Hong Ng, V.M., Wang, F., Xiao, Z., Li, C., Kong, L.B., Que, W., Zhou, K.: Synthesis and application of iron-based nanomaterials as anode of lithium-ion batteries and supercapacitors. J. Mater. Chem. A **6**, 9332–9367 (2018)
27. Nguyen, T., Montemor, M.D.F.: Metal oxide and hydroxide-based aqueous supercapacitors: from charge storage mechanisms and functional electrode engineering to need-tailored devices. Adv. Sci. **6**(9), 1801797 (2019)
28. Yang, J., Wang, H., Wang, R.: Facile synthesis of core–shell FeOOH@MnO_2 nanomaterials with excellent cycling stability for supercapacitor electrodes. J. Mater. Sci. Mater. Electron. **28**, 6481–6487 (2017)
29. Ratha, S., Vernekar, D., Sivaneri, K., Jagadeesan, D., Rout, C.S.: Iron-carbon nanohybrid particles as environmentally benign electrode for supercapacitor. J. Solid. State Electrochem. **21**, 1665–1674 (2017)
30. Mathevula, L.E., Noto, L.L., Mothudi, B.M., Chithambo, M., Dhlamini, M.S.: Structural and optical properties of sol–gel derived α-Fe_2O_3 nanoparticles. J. Lumin. **192**, 879–887 (2017)
31. Narayanaswamy, V., Obaidat, I.M., Kamzin, A.S., Latiyan, S., Jain, S., Kumar, H., Srivastava, C., Alaabed, S., Issa, B.: Synthesis of graphene oxide–Fe_3O_4 based nanocomposites using the mechanochemical method and in vitro magnetic hyperthermia. Int. J. Mol. Sci. **20**(13), 3368 (2019)
32. Ramzannezhad, A., Gill, P., Bahari, A.: Fabrication of magnetic nanorods and their applications in medicine. BioNanoMaterials **18**(3–4), 20170008 (2017)
33. Li, J., Shi, X., Shen, M.: Hydrothermal synthesis and functionalization of iron oxide nanoparticles for MR imaging applications. Part. Part. Syst. Charact. **31**(12), 1223–1237 (2014)
34. Erfani Gahrouei, Z., Imani, M., Soltani, M., Shafyei, A.: Synthesis of iron oxide nanoparticles for hyperthermia application: effect of ultrasonic irradiation assisted co-precipitation route. Adv. Nat. Sci. Nanosci. Nanotechnol. **11**, 025001 (2020)
35. Darvina, Y., Yulfriska, N., Rifai, H., Dwiridal, L., Ramli, R.: Synthesis of magnetite nanoparticles from iron sand by ball-milling. J. Phys. Conf. Ser. **1185**, 012017 (2019)
36. Ozcelik, B., Ergun, C.: Synthesis and characterization of iron oxide particles using spray pyrolysis technique. Ceram. Int. Part A **41**(2), 1994–2005 (2015)
37. Kazeminezhad, I., Mosivand, S.: Phase transition of electro oxidized Fe_3O_4 to γ and α-Fe_2O_3 nanoparticles using sintering treatment. Acta Phys. Pol. A **125**, 1210–1214 (2014)

38. Zdorovets, M.V., Kozlovskiy, A.L., Fadeev, M.S., Egizbek, K.B., Rusakov, V.S., Gubaidulina, T.V., Kadyrzhanov, K.K.: The effect of electron irradiation on the structure and properties of α-Fe_2O_3 nanoparticles as cathode material. Ceram. Int. **46**(9), 13580–13587 (2020)
39. Torres-Gómez, N., Nava, O., Argueta-Figueroa, L., García-Contreras, R., Baeza-Barrera, A., Vilchis-Nestor, A.R.: Shape tuning of magnetite nanoparticles obtained by hydrothermal synthesis: effect of temperature. J. Nanomater. (2019). https://doi.org/10.1155/2019/7921273
40. Guellati, O., Harat, A., Momodu, D., Dangbegnon, J., Romero, T., Begin, D., Pham-Huu, C., Manyala, N., Guerioune, M.: Electrochemical measurements of 1D/2D/3D Ni–Co bi-phase mesoporous nanohybrids synthesized using free-template hydrothermal method. Electrochim. Acta. **275**, 155–171 (2018)
41. Wu, H., Wu, G., Wang, L.: Peculiar porous α-Fe_2O_3, γ-Fe_2O_3 and Fe_3O_4 nanospheres: facile synthesis and electromagnetic properties. Powder Technol. **269**, 443–451 (2015)
42. Wang, L., Lu, X., Han, C., Lu, R., Yang, S., Song, X.: Electrospun hollow cage-like α-Fe_2O_3 microspheres: synthesis, formation mechanism, and morphology-preserved conversion to Fe nanostructures. CrystEngComm **16**, 10618–10623 (2014)
43. Singha, B.P., Kumar, A., Areizaga-Martinez, H.I., Olivencia, C.A.V., Tomar, M.S.: Synthesis, characterization, and electrocatalytic ability of γ-Fe_2O_3 nanoparticles for sensing acetaminophen. Indian J. Pure Appl. Phys. **55**, 722–728 (2017)
44. Anta, M.T., Ramos-docampo, M.A., Comesaña-Hermo, M., Rivas-Murias, B., Salgueiriño, V.: Raman spectroscopy to unravel the magnetic properties of iron oxide nanocrystals for biorelated applications. Nanoscale Adv. **1**, 2086–2103 (2019)
45. Hedenstedt, K., Backstr, J., Ahlberg, E.: In-situ Raman spectroscopy of α- and γ-FeOOH during cathodic load. J. Electrochem. Soc. **164**(9), H621–H627 (2017)
46. Habib, N., Guellati, O., Nait-Merzoug, A., El Haskouri, J., Momodu, D., Manyala, N., Begin, D., Guerioune, M.: Ni–Zn hydroxide-based bi-phase multiscale porous nanohybrids: physico-chemical properties. Appl. Nanosci. **275**, 1–11 (2019)
47. Barik, R., Jena, B.K., Mohapatra, M.: Metal doped mesoporous FeOOH nanorods for high performance supercapacitors. RSC Adv. **7**, 49083–49090 (2017)
48. Arjomandi, J., Yong, J., Movafagh, R., Moghanni-bavil-olyaei, H., Parvin, M.H.: Polyaniline/aluminum and iron oxide nanocomposites supercapacitor electrodes with high specific capacitance and surface area. J. Electroanal. Chem. **810**, 100–108 (2018)
49. Khan, I., Saeed, K., Khan, I.: Nanoparticles: properties, applications and toxicities. Arab. J. Chem. **12**(7), 908–931 (2019)
50. Barakat, N.A.M.: Synthesis and characterization of maghemite iron oxide (γ-Fe_2O_3) nanofibers: novel semiconductor with magnetic feature. J. Mater. Sci. **47**, 6237–6245 (2012)
51. Bashir, A.K.H., Mayedwa, N., Kaviyarasu, K., Razanamahandry, L.C., Matinise, N., Bharuth-Ram, K., Tchoula Tchokonté, M.B., Ezema, F.I., Maaza, M.: Investigation of electrochemical performance of the biosynthesized α-Fe_2O_3 nanorods. Surf. Interfaces **17**, 100345 (2019)
52. Palagiri, B., Chintaparty, R., Nagireddy, R.R., Reddy, V.S.R.I.: Influence of synthesis conditions on structural, optical and magnetic properties of iron oxide nanoparticles prepared by hydrothermal method. Phase Transit. **90**(6), 578–589 (2017)
53. Viter, R., Iatsunskyi, I.: Optical spectroscopy for characterization of metal oxide nanofibers. In: Barhoum, A., Bechelany, M., Makhlouf, A. (eds.) Handbook of Nanofibers, pp. 1–35. Springer, Cham (2018)
54. Ma, J., Guo, X., Yan, Y., Xue, H., Pang, H.: FeO_x-based materials for electrochemical energy storage. Adv. Sci. **5**(6), 1700986 (2018)
55. Kennaz, H., Harat, A., Guellati, O., Momodu, D.Y., Barzegar, F., Dangbegnon, J.K., Manyala, N., Guerioune, M.: Synthesis and electrochemical investigation of spinel cobalt ferrite magnetic nanoparticles for supercapacitor application. J. Solid State Electrochem. **22**, 835–847 (2018)
56. Xu, B., Zheng, M., Tang, H., Chen, Z., Chi, Y., Wang, L., Zhang, L., Chen, Y., Pang, H.: Iron oxide-based nanomaterials for supercapacitors. Nanotechnology **30**, 204002 (2019)
57. Chaudhari, N.K., Chaudhari, S., Yu, J.S.: Cube-like α-Fe_2O_3 supported on ordered multimodal porous carbon as high performance electrode material for supercapacitors. Chemsuschem **7**(11), 3102–3111 (2014)
58. Duan, C., Zhu, F., Wang, C., Ke, X., Ren, G., Meng, Y.: 3D Porous iron oxide/carbon with large surface area as advanced anode materials for lithium-ion batteries. Ionics (2020). https://doi.org/10.1007/s11581-020-03574-w
59. Zhang, M., Chen, K., Chen, X., Peng, X., Sun, X., Xue, D.: Crystallization of FeOOH via iron salts: an anion chemoaffinity controlled hydrolysis toward high performance inorganic pseudocapacitor materials. CrystEngComm **17**, 1917–1922 (2015)
60. Luo, H., Tao, K., Gong, Y.: K-doped FeOOH/ Fe_3O_4 nanoparticles grown on stainless steel substrate with superior and increasing specific capacity. Dalton Trans. **48**, 2491–2504 (2019)
61. Xu, J.S., Zhu, Y.J.: Monodisperse Fe_3O_4 and γ-Fe_2O_3 magnetic mesoporous microspheres as anode materials for lithium-ion batteries. ACS Appl. Mater. Interfaces **4**, 4752–4757 (2012)
62. Prasanna, B.P., Avadhani, D.N., Raghu, M.S., Kumar, Y.: Synthesis of polyaniline/α-Fe_2O_3 nanocomposite electrode material for supercapacitor applications. Mater. Today Commun. **12**, 72–78 (2017)
63. Laviron, E.: General expression of the linear potential sweep voltammogram in the case of diffusionless electrochemical systems. J. Electroanal. Chem. Interfaces Electrochem. **101**(1), 19–28 (1979)
64. Shanmugavani, A., Selvan, R.K.: Microwave assisted reflux synthesis of $NiCo_2O_4$/NiO composite: Fabrication of high performance asymmetric supercapacitor with Fe_2O_3. Electrochim. Acta. **189**, 283–294 (2016)
65. Nithya, V.D., Arul, N.S.: Review on α-Fe_2O_3 based negative electrode for high performance supercapacitors. J. Power Sources **327**, 297–318 (2016)
66. Jiao, Y., Liu, Y., Yin, B., Zhang, S., Qu, F., Wu, X.: Hybrid α-Fe_2O_3@NiO heterostructures for flexible and high performance supercapacitor electrodes and visible light driven photocatalysts. Nano Energy **10**, 90–98 (2014)
67. Sarno, M., Ponticorvo, E., Cirillo, C.: High surface area monodispersed Fe_3O_4 nanoparticles alone and on physical exfoliated graphite for improved supercapacitors. J. Phys. Chem. Solids **99**, 138–147 (2016)
68. Zhang, S., Wang, X., Li, Y., Mu, X., Zhang, Y., Du, J., Liu, G., Hua, X., Sheng, Y., Xie, E., Zhang, Z.: Facile synthesis of carbon nanotube-supported NiO/Fe_2O_3 for all-solid-state supercapacitors. Beilstein J. Nanotechnol. **10**, 1923–1932 (2019)
69. Shou, Q., Cheng, J., Zhang, L., Nelson, B.J., Zhang, X.: Synthesis and characterization of a nanocomposite of goethite nanorods and reduced graphene oxide for electrochemical capacitors. J. Solid State Chem. **185**, 191–197 (2012)